Sol-gel synthesis of magnetic TiO2 microspheres and characterization of their in vitro heating ability for hyperthermia treatment of cancer

doi: 10.1007/s10971-015-3680-x

Sol-gel synthesis of magnetic TiO_2 microspheres and characterization of their *in vitro* heating ability for hyperthermia treatment of cancer

GENGCI LIU[1]*, MASAKAZU KAWASHITA[1], ZHIXIA LI[2],

TOSHIKI MIYAZAKI[3], HIROYASU KANETAKA[4]

[1] *Graduate School of Biomedical Engineering, Tohoku University, Sendai 980-8579, Japan*

[2]*School of Chemistry and Chemical Engineering, Guangxi University, Nanning 530004, China*

[3]*Graduate School of Life Science and Systems Engineering, Kyushu Institute of Technology, Kitakyushu 808-0196, Japan*

[4] *Liaison Center for Innovative Dentistry, Graduate Schools of Dentistry, Tohoku University, Sendai 980-8575, Japan*

*Corresponding author：GENGCI LIU E-mail: liugengci@ecei.tohoku.ac.jp

Abstract. Common cancer treatments are invasive and lack specificity, leading to unwanted side effects. Because hyperthermia can kill cancer cells and damage proteins and structures within cells, it has been considered a novel, minimally invasive cancer treatment. However, many hyperthermia treatments cannot heat deep-seated tumors effectively and locally. Heat-generating, magnetic microspheres can help address this challenge. However, current research has not produced microspheres that can be sufficiently heated. We prepared magnetic titania (TiO_2) microspheres by introducing magnetite nanoparticles (MNPs) into the sol-gel process during water-in-oil emulsion for *in situ* hyperthermia treatment of cancers. Two types of MNPs were used in this study: one type was synthesized by a chemical coprecipitation method, and the other type was commercially available MNPs. The obtained microspheres contained up to 46.7 wt% MNPs, and their saturation magnetization and coercive force were 34.2 emu/g and 103 Oe, respectively. The particles' *in vitro* heating efficiency in an agar phantom was measured in an alternating magnetic field of 300 Oe and 100 kHz. The temperature increase of the agar phantom within 300 s was 4.5ºC for microspheres with MNPs that were synthesized by chemical coprecipitation and 53°C for microspheres with commercially available MNPs. The excellent heating efficiency of the microspheres may be attributed to the hysteresis losses of the magnetic particles. These microspheres are believed to be promising thermoseeds for hyperthermic treatment of cancer.

Keywords: sol-gel process, magnetite, titania microspheres, hyperthermia treatment of cancer

1. Introduction

Hyperthermia is a novel and minimally invasive type of cancer treatment in which body tissue is exposed to high temperatures (up to 43ºC) [1]. Tumor cells have difficulty in dissipating heat, because of their disorganized and compact vascular structure [2]. Research has shown that cancer cells can be damaged and killed at 43 ºC or higher, but normal cells are not damaged up to approximately 48 ºC [3]. Several methods of hyperthermia have been studied, and different types of external heat treatments for cancer have been attempted [4]. However, a major disadvantage of these techniques is that they cannot effectively heat deep-seated tumors. Magnetic microspheres with a diameter of 20–30 μm are potentially the only means of generating hyperthermia for deep-seated tumors without causing significant side effects in normal cells. Microspheres transported through the blood vessels can be entrapped in the capillary bed of the tumors. From their hysteresis loss and/or relaxation loss under an alternating current (AC) magnetic field, the microspheres can heat tumor cells locally [5-6]. In addition, the microspheres in the capillary bed of tumors can provide therapeutic effects through embolization, which would prevent the transport of blood and nutrition supply to the tumors [7].

To date, several groups have developed magnetite (Fe_3O_4)-containing glass ceramics for this purpose, including magnetite Fe_3O_4 in a matrix of β-wollastonite (β-$CaSiO_3$) and Fe_3O_4 in a B_2O_3-free $CaO–SiO_2–P_2O_5$ glassy phase [8-9]. However, none of the microspheres have been produced to have a diameter of 20–30 μm or have exhibited a high heat-generating ability. In our previous studies [10], we prepared magnetic SiO_2 microspheres with a diameter of 20–30 μm using a sol-gel method, which showed a higher specific absorption rate. Titania (TiO_2) might show better biocompatibility than SiO_2. Actually, it has been reported that osteoblast differentiation is enhanced

on TiO_2-coated scaffold than SiO_2-coated scaffold [11] and TiO_2-containing bone cement shows a good bone-bonding ability *in vivo* [12,13].We previously tried to prepare magnetic TiO_2 microspheres for hyperthermic treatment of cancer [14] and the particle size was controlled by optimizing the reaction conditions, i.e., the molecular ratio of the reactants and the stirring speed, but the content of magnetic materials was not sufficiently high, and the diameter of the microspheres was too small for embolic therapy.

In the present study, we prepared magnetic TiO_2 microspheres with a high content of magnetite nanoparticles (MNPs) using a sol-gel process in a water-in-oil emulsion. The structure and magnetic properties of the resultant microspheres were characterized. We also measured the *in vitro* heating ability of the microspheres under an AC magnetic field.

2. Materials and methods

It has been reported that MNPs show different heating behaviors depending on their size. Therefore, in this study, we used two different-sized particles: a) MNPs prepared by coprecipitation method (COP) [15] and b) commercially available MNPs (SA) (Sigma-Aldrich Corporation, St. Louis, USA).

2.1 Preparation of TiO_2 microspheres containing MNPs

The oil phase consisted of 54 g of kerosene, 4.5 g of sorbitan monooleate (span 80), and 1.5 g of sorbitan monostearate (span 60). The oil phase was placed in a water bath and heated to 30ºC for 20 min while being stirred with a homogenizer at approximately 1,600 rpm. The MNPs (COP and

SA; 1 g or 2 g) were then introduced into the oil phase along with 4.2 mL of H_2O while being vigorously stirred. The water phase, which consisted of 2.7 g of methanol (CH_3OH), 4.5 g of titanium tetraisopropoxide (TTIP), and 3 g of diethanolamine (DEA) was added to the stirred solution. Then, the emulsification process began with 20 min at 30ºC, followed by 20 min at 40ºC and 2 h at 55ºC. The gel particles were separated by centrifugation at 3,000 rpm for 5 min and washed with ethanol four times. Then, the gel particles were dried at 36.5ºC for 12 h and at 150ºC for 3 h. The dried gel particles were further heated to 500ºC at a slow rate (48ºC/h from room temperature to 500ºC), kept at 500ºC for 3 h, and allowed to cool in the same atmosphere. As a reference, we also prepared TiO_2 microspheres without MNPs. Unless indicated, all reagents used were obtained from Wako Pure Chemical Industries, Osaka, Japan.

To explore optimal heating efficiencies, we prepared 4 types of magnetic TiO_2 microspheres with different amounts (1 g or 2 g) and different types (COP or SA) of MNPs. Table 1 shows the compositions and characteristics of four different samples (COP-1g, COP-2g, SA-1g, and SA-2g) obtained from these procedures.

2.2 Characterization of the samples

The crystalline phase of the samples was verified by powder X-ray diffraction (XRD; Miniflex 600HDA, Rigaku, Japan) using the following settings: X-ray source, CuKα; X-ray power, 40 kV, 15 mA; scanning rate, 2 θ = 10° /min. The average crystallite size of the MNPs was estimated using Scherrer's formula [16]. To estimate of the average oxidation state for iron in the microspheres, quantitative analysis by powder diffraction was performed using an integrated X-ray Powder Diffraction Software Package (PDXL; Rigaku, Version 2.1.3.4) with Whole Powder Pattern

Fitting (WPPF) [17-18], connected to ICDD-PDF-2. The particle sizes and crystal morphologies of the samples were observed using a scanning electron microscope (SEM; VE-8800, Keyence, Japan), transmission electron microscopy (TEM; CM200FEG, Philips, Netherlands) and particle size distribution analyzer (PSD; Microtrac HRA (9320-X100), Nikkiso, Japan).

2.3 Magnetic properties measurement

The saturation magnetization (*Ms*) and coercive force (*Hc*) of the samples were measured using a vibrating sample magnetometer (VSM-5, Toei, Japan) in magnetic fields up to 10 kOe at room temperature at a frequency of 80 Hz. We assumed that the area of the hysteresis loop measured under the applied magnetic field (100 kHz, 300 Oe) was the same as that measured in a field of 300 Oe using the VSM. The heat generated by the samples was calculated using the following equation [19]:

$$P = f \oint HdB \times 10^{-7}, \qquad (1)$$

where f is the frequency (in Hz), H is the magnetic field strength (in Oe), and B is the magnetization (in emu) of a sample in an applied magnetic field. The term $\oint HdB$ is the area of the hysteresis loop in the applied magnetic field. Therefore, in our calculations, f = 100 kHz and the area of the hysteresis loop measured at 300 Oe using the VSM was substituted for $f \oint HdB$.

2.4 *In vitro* heat-generating ability measurement

A sample (0.2 g) was dispersed into 3 mL of hot agar solution (agar content = 1.0 wt%) in a glass tube, and then the agar was solidified in cold water. The concentration of the sample in the agar phantom was 67 mg/mL. The glass tubes containing the samples were placed in an applied AC magnetic field of 100 kHz and 300 Oe, in accordance with our previous study [10]. The heat

generated by the samples was investigated by measuring the change in temperature of the agar phantom as a function of time using a fiber optic temperature sensor (TempSens, Opsens Inc., Canada).

3. Results and discussion

3.1 Characterization and analysis (XRD, SEM, PSD)

Figure 1 shows the XRD patterns of all the samples in comparison with those of COP and SA. Sharp diffraction peaks of COP and SA were ascribed to magnetite (Fe_3O_4; PDF: 19-0629) and/or maghemite (γ-Fe_2O_3; PDF: 39-1346). Sharp diffraction peaks of COP-1g, COP-2g, SA-1g, and SA-2g were ascribed to magnetite Fe_3O_4 and/or γ-Fe_2O_3, hematite (α-Fe_2O_3; PDF: 33-0664), and anatase-type TiO_2 (PDF: 21-1272). These results indicate that magnetic nanoparticle-containing TiO_2 microspheres were obtained. The crystallite sizes of COP and SA was estimated to be 10.5 and 24.3 nm, respectively. Figure 2 shows the analysis of the oxidation state of iron by WPPF. The γ-Fe_2O_3 content of COP-Xg magnetic TiO_2 microsphere samples was higher than that of SA-Xg (X: 1 or 2). A portion of the MNPs was oxidized to non-magnetic α-Fe_2O_3 because the heat treatment of the samples was conducted in air. However, the lack of oxygen in the heating process would have inhibited crystallization of TiO_2 in the microspheres [20]. Therefore, further work will be performed to obtain magnetic microspheres without hematite by applying heat treatment in an oxygen-controlled atmosphere.

Figure 3 shows SEM photographs of SA-1g, SA-2g, COP-1g, and COP-2g. Irrespective of the MNP content and type, spherical microspheres with a diameter of approximately 8-10 μm were obtained by the present method. In the size distribution curves of the samples (Figure 4), there was

one apex in the range of 7 μm to 15 μm for the COP-1g, COP-2g, and SA-1g samples. Sample SA-2g showed a wider aggregate size distribution, possibly because of incomplete hydrolysis and polycondensation reaction of TTIP [14]. The obtained microspheres had a very rough surface, probably because because there were also some non-spherical and small spherical particles. However, the 8 μm microspheres were not large enough to be embolic agents. Particles with small sizes may travel too far from the point of interest and cause non-targeted embolization [21]. Hence, the next stage of our the research should focus on controlling the particle size to 20–30 μm by optimizing reaction conditions such as the molecular ratio of the reactants, the stirring speed, and the species and concentration of the surfactants.

3.2 TEM characterization and analysis of magnetic nanoparticles

Figure 5 shows TEM images of COP and SA. COP contained nearly spherical particles with a diameter of approximately 10-15 nm. SA was composed of cube-shaped particles with a few spherical particles sized approximately 30-40 nm. Because of the magnetic dipolar interactions of the nanoparticles [22-24], agglomeration of the particles occurred in both samples. Therefore, the observed results were slightly larger than the size calculated from the Scherrer's equation. According to the reported values [25-26] for Fe_3O_4, the single domain particle size was roughly estimated to be 80-150 nm. Therefore, according to the results calculated from Scherrer's formula and the observation results from the TEM images, the magnetic nanoparticles used in this experiment (COP and SA) consisted of single-domain particles.

3.3 Magnetic properties of samples

Figure 6 shows the magnetization curves of SA-1g, SA-2g, COP-1g, COP-2g, COP, and SA measured at 10 kOe. The magnetic properties of the obtained samples are summarized in Table 2.

Both COP and SA showed hysteresis loops in their respective magnetization curves, indicating the ferrimagnetic nature of the Fe_3O_4 particles. The *Ms* was determined by the magnetization curves under the applied field of 10 kOe. The COP composed of smaller MNPs exhibited a smaller *Ms* than SA, probably because of surface spin disorder [27] caused by cation redistribution or the formation of spin glass-like structure in the near-surface layers. The decrease in particle size causes an increasing proportion of spin disordered surface layers [28]. Thus, smaller particles possess lower magnetization. The *Ms* of SA-1g and SA-2g was 21.5 and 34.2 emu/g, respectively, which was lower than that of the starting SA (73.2 emu/g). The *Ms* of COP-1g and COP-2g was 5.7 and 10.2 emu/g, respectively, which was lower than that of the starting COP (64.8 emu/g). There are three possible explanations for the decrease in *Ms* of SA-1g, COP-1g, SA-2g, and COP-2g. The first is simply related to the content of MNPs in the microspheres. The amount of MNPs per unit weight of microspheres decreased when the amount of MNPs used in the synthesis decreased. The second reason is that the mass of the TiO_2 shell is much larger than that of the MNPs inside. However, TiO_2 does not exhibit magnetic properties, which leads to a lower density of magnetic components in the SA-1g, COP-1g, SA-2g, and COP-2g. The third reason is that the coating layer on the MNPs weakens the superexchange interaction between the magnetic moments on iron ions and induces spin disorder on the surface of nanoparticles, which results in a lower *Ms* compared to that of the starting MNPs [29-30]. The coercive force is significantly influenced by the crystal dimensions. The *Hc* of SA (98.0 Oe) was approximately five times higher than that of COP (16.9 Oe). Similar results of other MNPs have been reported and attributed to their domain structures [31]. The *Hc* of SA-1g and SA-2g was 100 and 103 Oe, respectively, which was almost equal to that of the starting SA (98.0 Oe). The *Hc* of COP-1g and COP-2g was 22.2 and 21.1 Oe, respectively, which was also slightly higher

than that of the starting COP (16.9 Oe). The coercive force showed little difference from the starting magnetic nanoparticles (SA and COP) in the present experiment because of the following two opposite effects: the TiO_2 shell encapsulating the magnetite particles screens and decreases the magnetic dipole coupling interactions between neighboring magnetic nanoparticles [32], thereby reducing the coercivity value from hysteresis loop measurements. In contrast, magnetite Fe_3O_4 in the starting magnetic nanoparticles was partially converted to γ-Fe_2O_3 during the sol–gel synthesis procedure. The γ-Fe_2O_3 converted from Fe_3O_4 is likely to be larger than Fe_3O_4. For a single-domain particle, the value of *Hc* increases with increasing particle size [33]. These factors could lead to an increase in coercivity value. In this experiment, these two effects appeared to neatly balance each other.

From the ratio of the *Ms* of the samples to that of the starting MNPs (Table 2), the content of MNPs in the SA-1g, COP-1g, SA-2g, and COP-2g was calculated to be 29.4, 8.4, 46.7, and 15.7 wt%, respectively. MNPs generated from COP showed poor dispersibility in water and hence were lost as residue in the beaker. In contrast, SA MNPs did not have such a problem. Therefore, the MNP contents of SA-1g, and SA-2g were higher than those of COP-1g and COP-2g.

3.4 *In vitro* heat-generating ability of samples

To prevent evaluation errors and to obtain absolute heating measurements, the specific absorption rate (*SAR*) of each sample was analyzed based on the *in vitro* heat generation of samples. Figure 7 shows the time-dependent temperature curves of the agar phantom under a magnetic field of 100 kHz and 300 Oe. The temperature increases (ΔT) of the agar phantom at 10 min were 0.8, 7.8, and 8.3ºC for SA-1g, COP-1g, and COP-2g, respectively. The ΔT of the agar phantom at 6 min was 63.3ºC for SA-2g.

As described in section 2.3, we assumed that the area of the hysteresis loop measured under the applied magnetic field (100 kHz, 300 Oe) was the same as that measured in a field of 300 Oe using the VSM. Figure 8 shows the magnetization curves of the SA-1g, SA-2g, COP-1g, COP-2g, COP, and SA measured at 300 kOe. The irregularities in the magnetization curves may be attributed to the presence of different magnetic phases of Fe_3O_4 and γ-Fe_2O_3. The heat generated by the samples (heat generation: *P)* calculated for all the samples is also listed in Table 3.

From the increase in temperature, the value of *SAR* was calculated using the following equation [34]:

$$SAR = \frac{\sum_i C_i m_i}{m_{sample}} \frac{\Delta T}{\Delta t}, \qquad (2)$$

where $C_i m_i$ is the heat capacity of each component whose temperature is increased in the applied magnetic field (C_{agar} = 4.2 J/g K, $C_{magnetite}$ = 0.62 J/g K, and $C_{titania}$ = 0.69 J/g K) [35]. The term $\Delta T/\Delta t$ is the largest gradient of the time-dependent temperature curve. The values of SAR calculated for all the samples are also listed in Table 3.

It is speculated that hysteresis loss mainly contributes to the heat generation of SA-1g and SA-2g because the *SAR* value of SA-1g (6.3 W/g) and SA-2g (18.3 W/g) was lower than the heat generation (*P*) (SA-1g: 16.3 W/g, SA-2g: 21.3 W/g) calculated from the area of hysteresis loop. We believe that the hysteresis loss provided substantial heating power, but the TiO_2 shell had a negative influence on heat transfer and thus reduced heating efficiency. In contrast, the values of *SAR* of COP-1g (2.5 W/g) and COP-2g (1.9 W/g) were higher than *P* (COP-1g: 0.3 W/g, COP-2g: 0.3 W/g). Magnetite nanoparticles with a single-domain structure can be heated by relaxation loss under an alternating magnetic field [36]. However, in this experiment, the power loss resulting from relaxation

was insufficient, probably because the starting COP primarily contained particles with a diameter of 10 nm as observed in the TEM image (Figure 5), which is similar to the single-domain size. The Néel relaxation loss and Brownian relaxation loss are associated with the magnetic moment rotations of the entire group of particles and among the individual particles, respectively. Each relaxation time is given by the following equations (3), (4), and (5) [37-38]:

$$\tau_N = \tau_0 \exp\frac{KV}{kT} \tag{3}$$

$$\tau_B = \frac{4\pi\eta R_H^{\ 3}}{kT} \tag{4}$$

$$\tau_{eff} = \frac{\tau_N \tau_B}{\tau_N + \tau_B} \tag{5}$$

where τ_B is the Brownian relaxation time, τ_N is the Néel relaxation time, τ_0 is the time constant ($\tau_0 = 10^{-9}$ s), k is Boltzmann's constant, K is the anisotropy constant ($K = 1.35 \times 10^4$ J/m), T is the temperature ($T = 293$ K), V is the particle volume (m^3), η is the viscosity (0.858 g/ms) [39], and R_H is the radius of the particle. The heat dissipation by relaxation loss is given by the following equation [40]:

$$P = \pi\mu_0\chi_0 H^2 f \frac{2\pi f\tau_{eff}}{1+(2\pi f\tau_{eff})^2} \tag{6}$$

where χ_0 is the AC magnetic susceptibility and H is the field amplitude (A/m). From calculations using Equation 3-6 at our given frequency, $\omega/2\pi$ =100 kHz, we estimated that Fe_3O_4 nanoparticles with a diameter of 14–25 nm would have power dissipation by relaxation loss under an alternating magnetic field of 100 kHz [41]. As discussed previously, Fe_3O_4 in the starting magnetic nanoparticles was partially converted to γ-Fe_2O_3 in the magnetic microsphere sample during the sol–gel synthesis procedure. The particle size of γ-Fe_2O_3 did not meet the criteria of being within 14–25 nm. Therefore,

the power loss resulting from relaxation decreased greatly. It is expected that microspheres with excellent heating capability can be obtained when Fe_3O_4 nanoparticles with the ideal size of 14–25 nm are used. However such Fe_3O_4 nanoparticles are not commercially available. They might be chemically synthesized [42], but they are often unstable in aqueous medium. Further study is needed to synthesize TiO_2 microspheres containing MNPs with the ideal particle size.

4. Conclusion

Magnetic TiO_2 microspheres with a diameter of 7-15 μm were obtained by directly introducing pre-formed magnetic MNPs into a sol-gel process from TTIP in water-in-oil emulsion. The magnetic TiO_2 microspheres containing Fe_3O_4 at a content higher than 46 wt% increased the temperature of the agar phantom to above 43°C in 3 min. They are expected to be useful for arterial embolization hyperthermic treatment of cancer, but control of their diameter is essential.

Acknowledgements

This work was partially supported by a research grant from the Magnetic Health Science Foundation, Fukuoka, Japan.

References

1. Sugihara T (1986) Gan-to-Tatakau-Hyperthermia. Kinpoudou, Kyoto.
2. Conway J, Anderson AP (1986) Clin Phys Physiol Meas 7:287-318
3. Cavaliere R, Ciocatto EC, Giovanella BC, Heidelberger C, Johnson RO, Margottini M, Mondovi B, Moricca G, Rossi-Fanelli (1967) Cancer 20:1351-1381
4. Overgaard K, Overgaard J (1972) Eur J Cancer 8:65-78
5. Li Z, Kawashita M, Araki N, Mitsumori M, Hiraoka M, Doi M (2011) J Biomater Appl 25:643-661
6. Kawashita M, Tanaka M, Kokubo T, Inoue Y, Yao T, Hamada S, Shinjo T (2005) Biomaterials 26:2231-2238
7. Kawashita M, Domi S, Saito Y, Aoki M, Ebisawa Y, Kokubo T (2008) J Mater Sci Mater Med 19:1897-1903
8. Kokubo T, Ebisawa Y, Sugimoto Y, Kiyama M, Ohura K,Yamamuro T, Hiraoka M, Abe M (1990) Bioceramics 3:213-223
9. Kawashita M, Iwahashi Y, Kokubo T, Yao T, Hamada S, Shinjo T (2004) J Ceram Soc Japan 112:373-379
10. Li Z, Kawashita M, Kudo T, Kanetaka H (2012) J Mater Sci Mater Med 23:2461-2469
11. Sunada, K., Kikuchi, Y., Hashimoto, K., & Fujishima, A. (1998). Environmental Science & Technology, 32(5), 726-728.
12. Goto K, Tamura J, Shinzato S, Fujibayashi S, Hashimoto M, Kawashita M, Kokubo T, Nakamura T, (2005) Biomaterials 26(33):6496-6505
13. Goto K, Hashimoto M, Takadama H, Tamura J, Fujibayashi S, Kawanabe K, Kokubo T, Nakamura T (2008) J Mater Sci Mater Med 19(3):1009-1016
14. Li Z, Kawashita M, Doi M (2010) J Ceram Soc Japan 118:467-473
15. Sun J, Zhou S, Hou P, Yang Y, Weng J, Li X, Li M (2007) J Biomed Mater Res A 80(2):333-341

16. Patterson AL (1939) Phys Rev 56(10):978-???（←終わりのページは？）
17. Dong YH, Scardi P (2000) J Appl Cryst 33(1):184-189
18. Toraya H (1986) J Appl Cryst 19(6):440-447
19. Luderer A A, Borrelli NF, Panzarino JN, Mansfield GR, Hess DM, Brown JL, Hahn EW (1983) Rad Res 94(1):190-198
20. Takahashi Y, Ohsugi A, Arafuka T, Ohya T, Ban T, Ohya Y (2000) J Sol-Gel Sci Tech 17(3):227-238
21. Vaidya S, Tozer KR, Chen J (2008) Semin Intervent Radiol 25:204-215
22. Li Z, Kawashita M, Araki N, Mitsumori M, Hiraoka M, Doi, M (2010) Mater Sci Eng C, 30(7):990-996
23. Gao J, Zhang B, Zhang X, Xu B (2006) Angew Chem 118(8):1242-1245
24. Chantrell RW, Bradbury A, Popplewell J, Charles SW (1982) J Appl Phys 53(3):2742-2744
25. Kneller EF, Luborsky FE (1963) J Appl Phys 34(3):656-658
26. Dunlop DJ (1973) J Geophys Res 78(11):1780-1793
27. Georgea M, Johna AM, Naira SS, Joyb PA, Anantharaman MR (2006) J Magn Magn Mater 302:190-195
28. Balakrishnan S, Bonder MJ, Hadjipanayis GC (2009) J Magn Magn Mater 321:117-122
29. Kaiser R, Miskolczy G (1970) J Appl Phys 41:1064-1072
30. Caizer C, Savii C, Popovici M (2003) Mater Sci Eng B 97:129-134
31. Šepelák V, Baabeb D, Mienertb D, Schultzec D, Krumeichd F, Litterstb FJ, Beckera KD (2003) J Magn Magn Mater 257:377-386
32. Marcelo G, Pérez E, Corrales T, Peinado C (2011) J Phys Chem C 115: 25247-25256
33. Schmiedeskamp J, Elmers HJ, Heil W, Otten EW, Sobolev Y, Kilian W, Rinneberg.H, Thömmes.T, Seifert.FZimmer J Sander- F. J. Zimmer (2006) Eur Phys J D 38(3):445-454
34. Zhang LY, Gu H, Wang XM (2007) J Magn Magn Mater 311:228-233

35. Standard thermodynamic properties of chemical substances(2000) by CRC press LLC p20 http://www.nist.gov/data/PDFfiles/jpcrdS2Vol11.pdf#search='25.+Standard+thermodynamic+properties+of+chemical+substances'. Accessed 08 Oct 2014
36. Motoyama J, Hakata T, Kato R, Yamashita N, Morino T, Kobayashi T, Honda H (2008) Biomagn Res Tech 4:1-9
37. Hergt R, Andrä W, Ambly C G, Hilger I, Kaiser W A, Richter U, Schmidt HG (1998) IEEE Trans Magn 34: 3745-3754
38. Debye P (1929) Polar molecules. Dover, New York
39. Atsumi T, Jeyadevan B, Sato Y, Tohji K (2006) J Magn Soc Japan 30:555-560
40. Landau LD, Lifshitz EM (1960) Course of Theoretical Physics: Vol.: 8: Electrodynamics of Continuous Medie , Pergamon Press, United Kingdom.
41. Kötitz R, Weitschies W, Trahms L, Semmler W (1999) J Magn Magn Mater 201(1):102-104
42. Xuan S, Wang F, Wang YXJ, Jimmy CY, Leung KCF (2010) J Mater Chem 20(24):5086-5094

Figure Caption

Figure 1. XRD patterns of samples in comparison with those of COP and SA.

Figure 2. Oxidation state of iron analyzed by the WPPF method.

Figure 3. SEM photographs of samples.

Figure 4. Size distribution curves of samples.

Figure 5. TEM photographs of COP and SA.

Figure 6. Hysteresis loops of samples measured with the maximum applied field of 10 kOe.

Figure 7. Time-dependent temperature curves of the agar phantom.

Figure 8. Hysteresis loops of samples measured with the maximum applied field of 300 Oe.

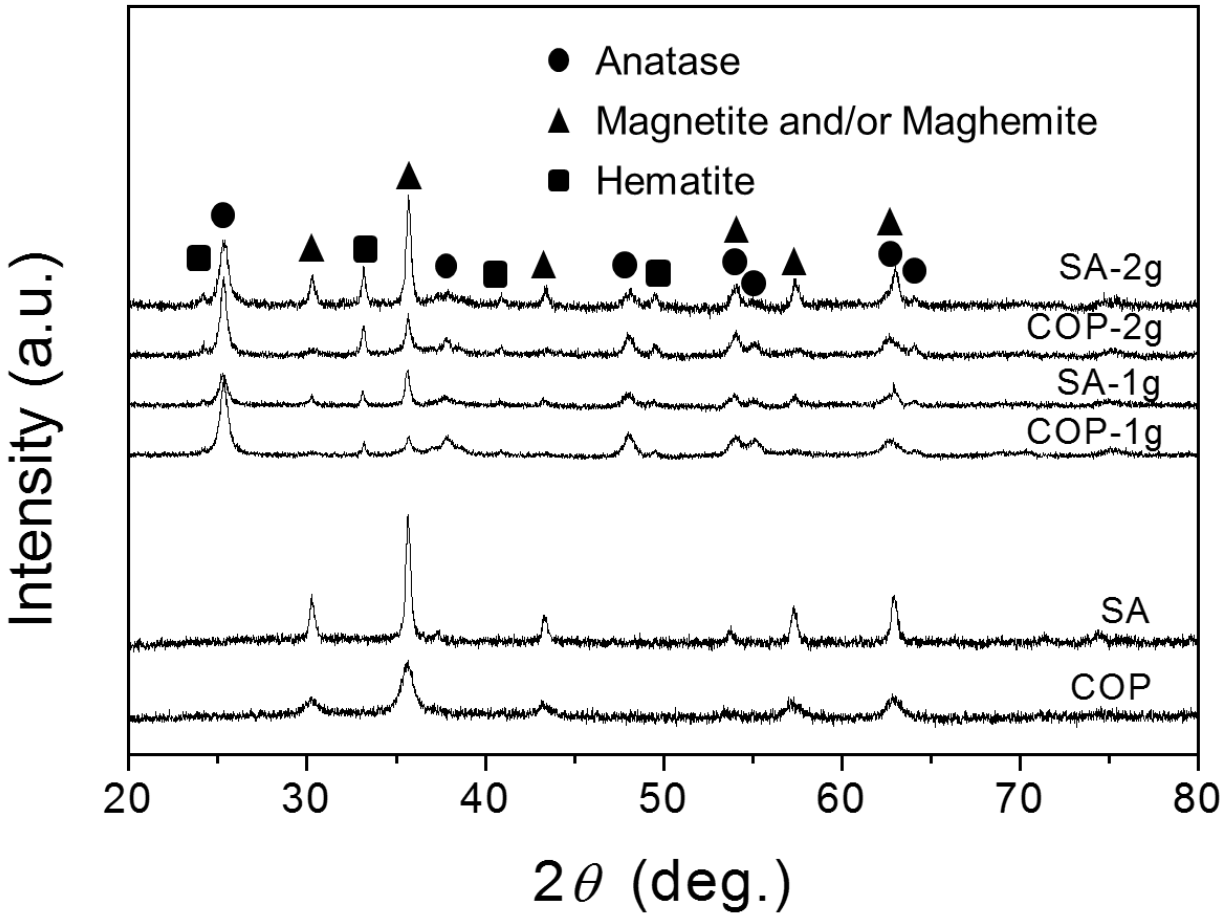

Figure 1. XRD patterns of samples in comparison with those of COP and SA.

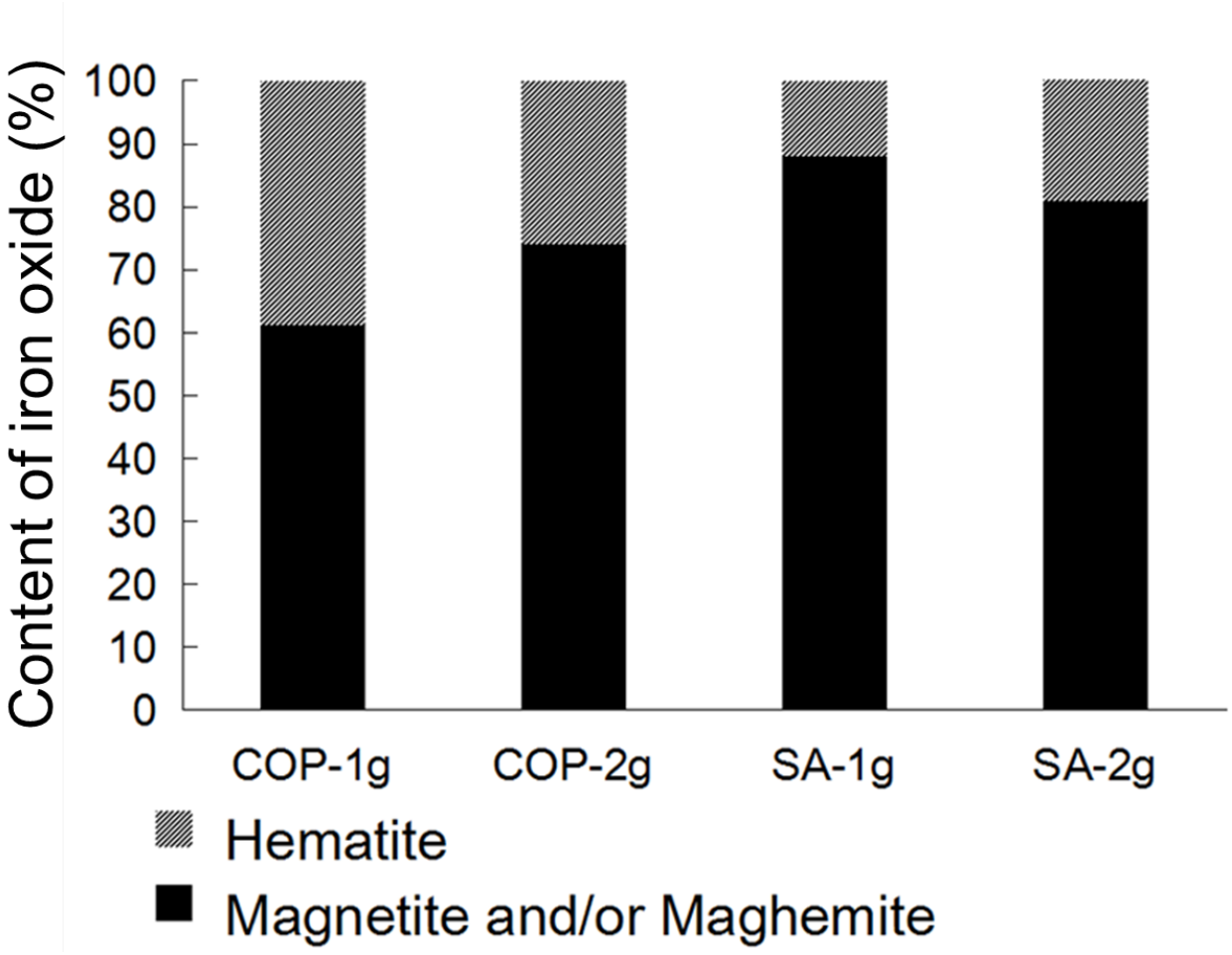

Figure 2. Oxidation state of iron analyzed by WPPF method.

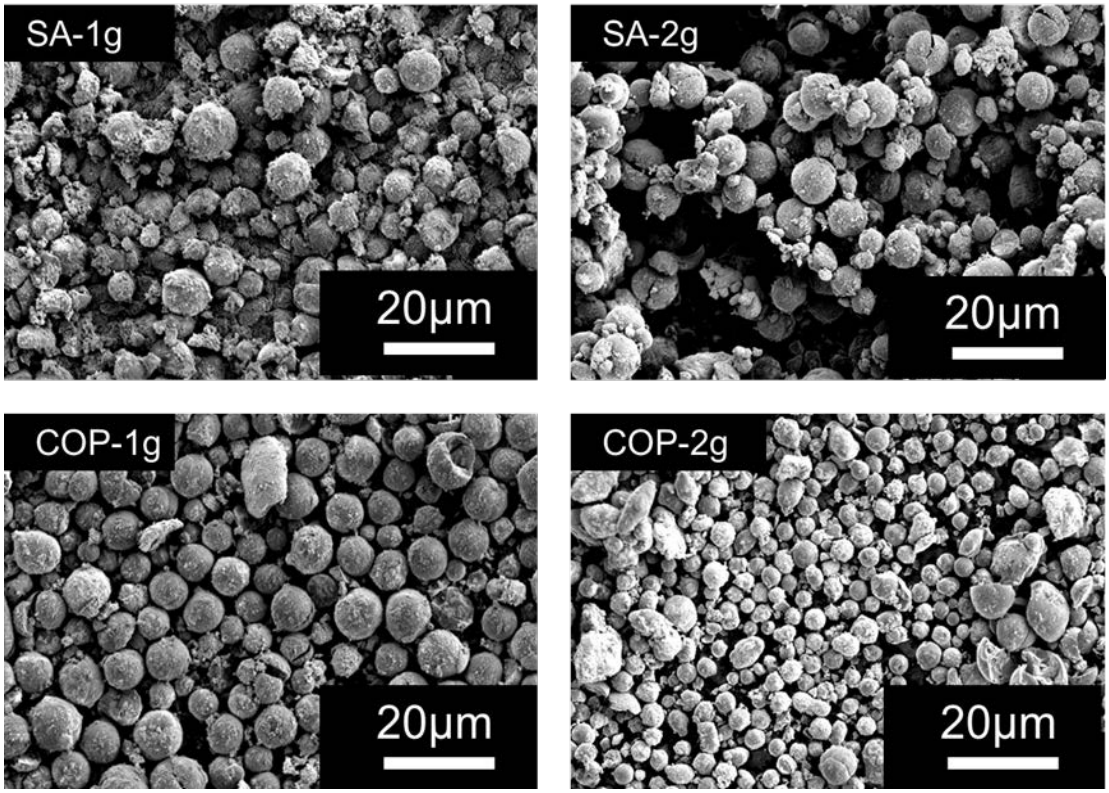

Figure 3. SEM photographs of samples.

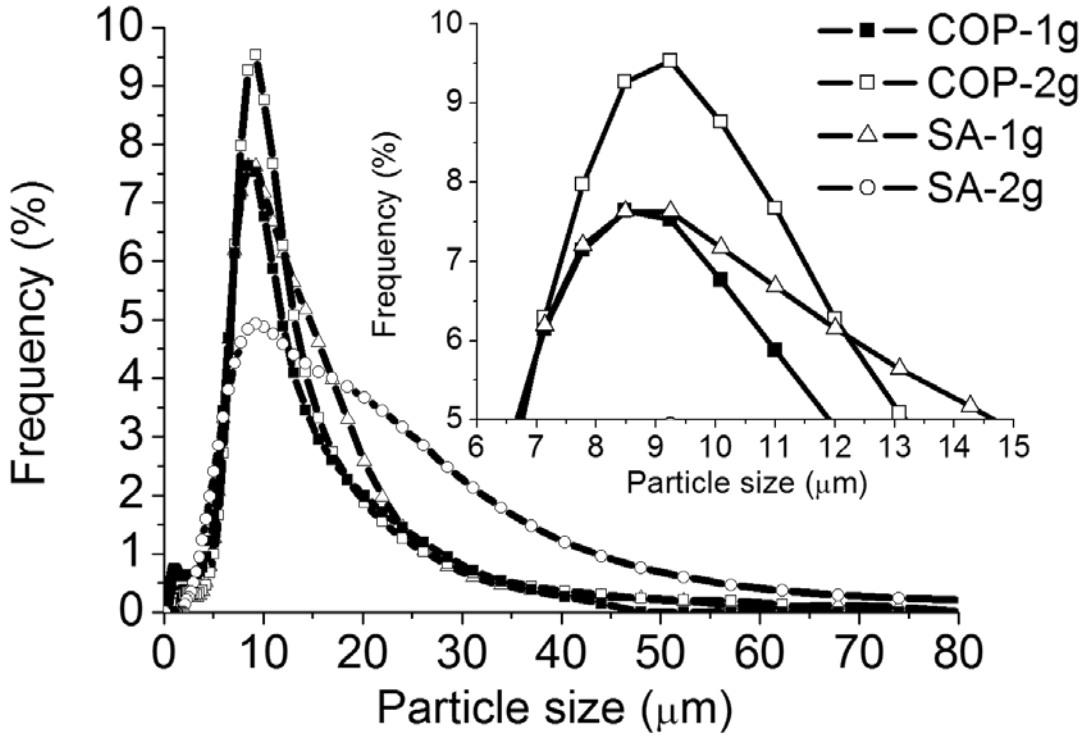

Figure 4. Size distribution curves of samples.

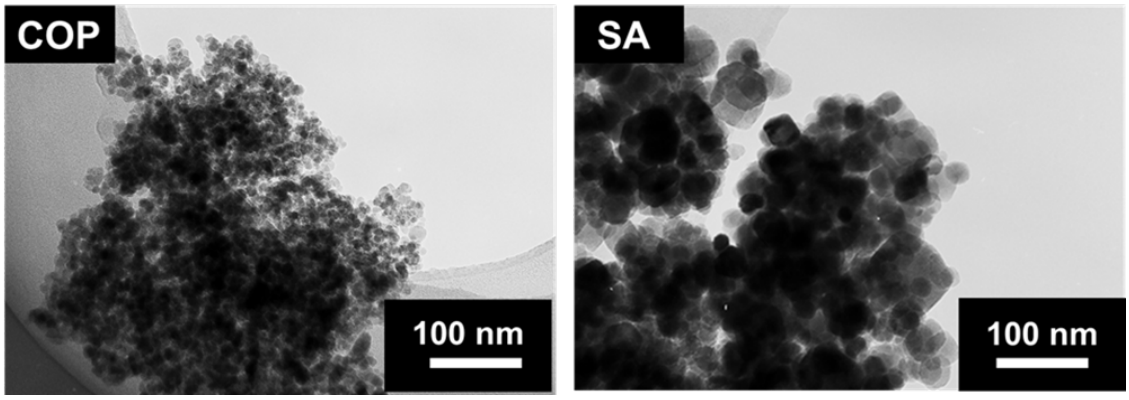

Figure 5. TEM photographs of COP and SA.

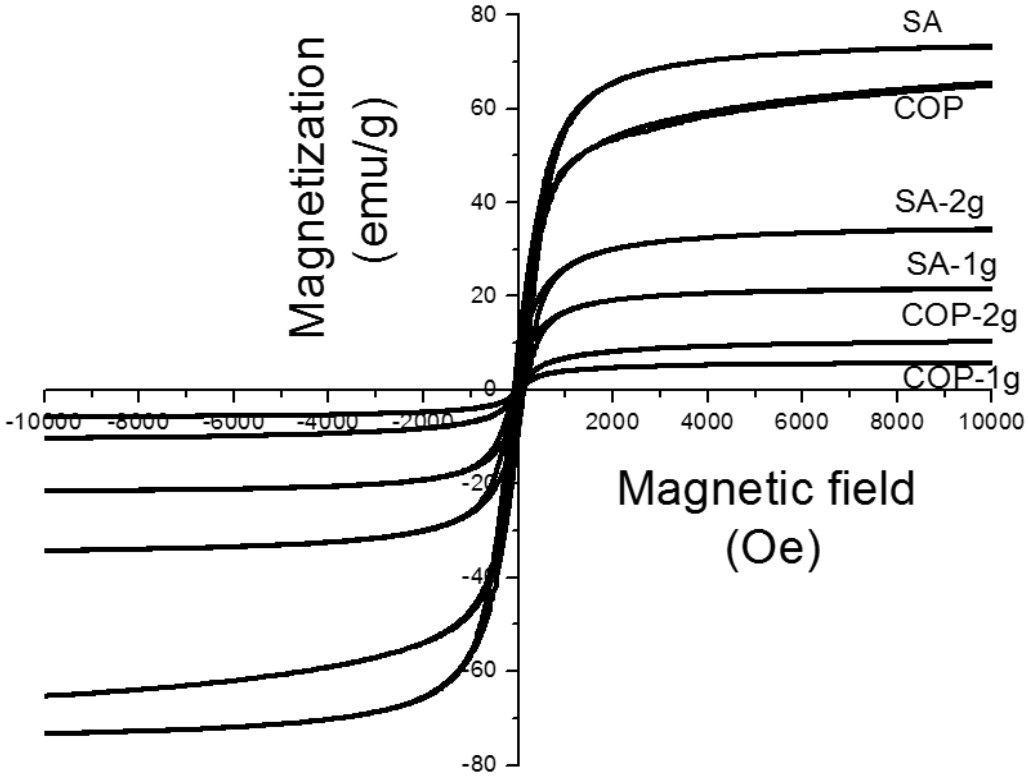

Figure 6. Hysteresis loops of samples measured with the maximum applied field of 10 kOe.

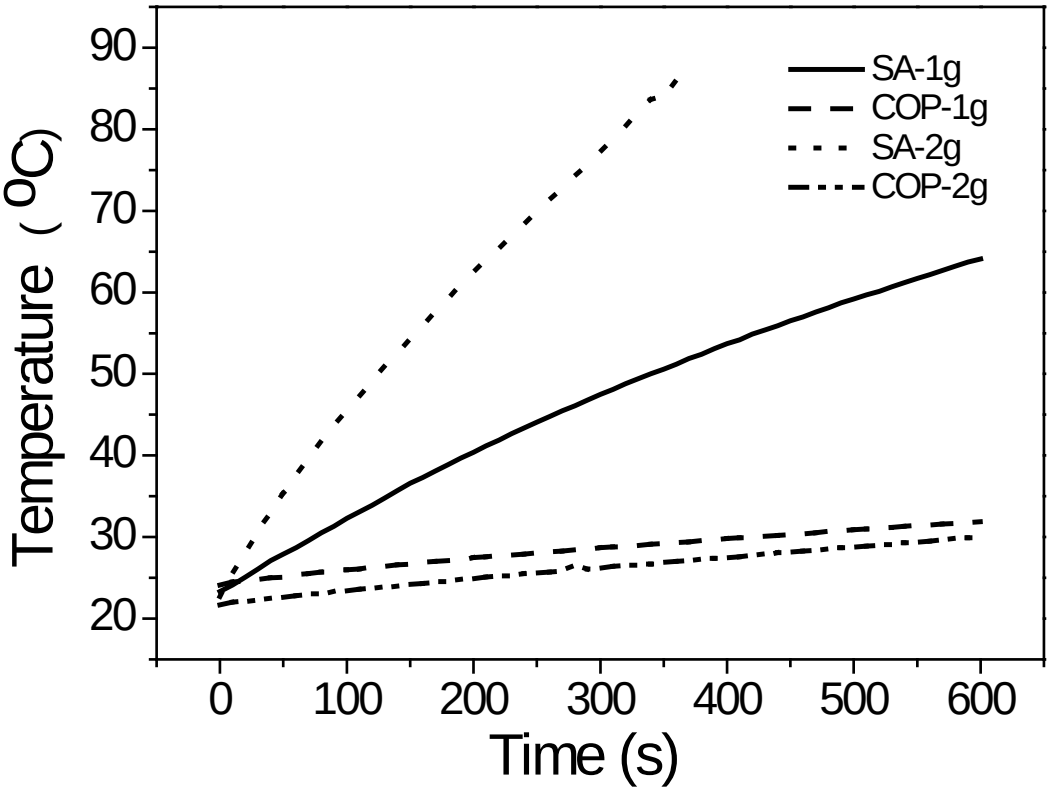

Figure 7. Time-dependent temperature curves of the agar phantom.

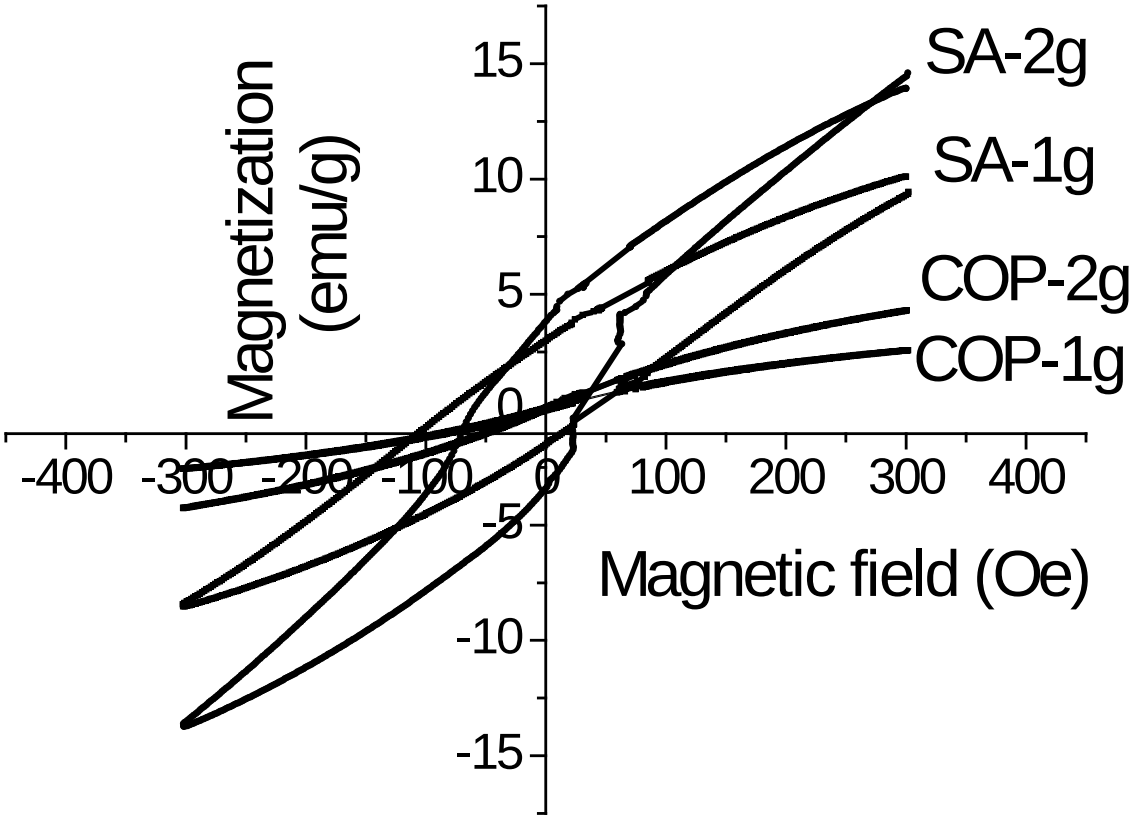

Figure 8. Hysteresis loops of samples measured with the maximum applied field of 300 Oe.

Table 1. Compositions and characteristics of samples and MNPs.

Sample	Type of MNPs	Amount of MNPs (g)
SA-1g	Ordered from Sigma-Aldrich®	1
COP-1g	Synthesized by coprecipitation method	1
SA-2g	Ordered from Sigma-Aldrich®	2
COP-2g	Synthesized by coprecipitation method	2
SA	Ordered from Sigma-Aldrich®	——
COP	Synthesized by coprecipitation method	——

Table 2. Magnetic properties and MNP contents of samples in comparison with MNPs.

Sample	*Ms* (emu/g)	*Hc* (Oe)	MNPs contents (wt%)
SA-1g	21.5	100.6	29.4
COP-1g	5.7	22.2	8.4
SA-2g	34.2	103.0	46.7
COP-2g	10.2	21.1	15.7
SA	73.2	98.0	--
COP	64.8	16.9	--

Table 3. Hysteresis loss and SAR value of samples

Sample	*P* (W/g)	*SAR* (W/g)
SA-1g	16.3	6.3
COP-1g	0.3	2.5
SA-2g	21.3	18.3
COP-2g	0.3	1.9